JOURNAL OF AIRCRAFT
Vol. 32, No. 2, March–April 1995

Impact of Aeroelastic-Propulsive Interactions on Flight Dynamics of a Hypersonic Vehicle

David L. Raney* and John D. McMinn*
NASA Langley Research Center, Hampton, Virginia 23681
and
Anthony S. Pototzky†
Lockheed Engineering and Sciences Company, Inc., Hampton, Virginia 23681

Many air-breathing hypersonic vehicle design concepts utilize the lower surface of an elongated fuselage forebody to provide aerodynamic compression for a supersonic combustion ramjet module, or a scramjet. This highly integrated design approach creates the potential for an unprecedented form of aeroelastic-propulsive interaction in which deflections of the vehicle fuselage give rise to propulsive force and moment variations that may impact the vehicle's flight dynamic characteristics. This investigation examines the potential for such interactions using a math model that describes the longitudinal flight dynamics, propulsion system, and first seven elastic modes of a hypersonic vehicle concept. Estimates of the propulsion system sensitivity to angle-of-attack variations and modal fuselage deflections are presented and compared with predictions based on an earlier reference. The combined aeroelastic-propulsive model is used to illustrate a variation in the vehicle's longitudinal flight dynamics with the propulsion system sensitivities. Numerical values for the completed model at flight conditions of Mach 6 and Mach 10 are presented.

Nomenclature

A = stability matrix
a_i = ith state in actuator model
B = control input matrix
C = mode shape matrix
h = altitude perturbation, in.
I = identity matrix
M = pitching moment, positive nose-up, ft-lb
u = control deflection, positive trailing-edge down, rad
X = axial force, positive forward, lb
x = vector of generalized elastic coordinates
$\dot{x}$ = state vector
y = output vector from state-space model
Z = normal force, positive upward, lb
α = angle of attack, deg
δ_j = vertical displacement due to elastic deflection at j inches from vehicle nose, in.
η_i = generalized coordinate corresponding to the ith elastic mode shape
θ = pitch attitude perturbation, rad

Introduction

THE desire to achieve orbit-on-demand access to space with rapid turnaround capability and aircraft-like processing operations has given rise to numerous hypersonic aerospace plane design concepts that would take off horizontally from a conventional runway and employ air-breathing scramjet propulsion systems for acceleration to orbital speeds. Most of these hypersonic vehicle concepts utilize the lower surface of an elongated fuselage forebody to achieve aerodynamic compression for a scramjet combustor module. This type of airframe-integrated propulsion system tends to be highly sensitive to inlet conditions and angle-of-attack perturbations.[1] Furthermore, the basic configuration of the fuselage produces relatively low-frequency elastic modes that may cause perturbations in combustor inlet conditions due to the oscillation of the forebody compression surface. These factors create the potential for an unprecedented form of interaction, whereby propulsion system sensitivities to aeroelastic fuselage deflections impact the vehicle's flight dynamic characteristics.

The propulsive force and moment variations resulting from aeroelastic-propulsive interactions may have an appreciable impact on the performance, guidance, and control of a hypersonic aerospace plane. Modeling this interaction will require a concerted aerodynamic, structural, and propulsion analysis effort, as emphasized in earlier research by McRuer.[2] The objective of this study is to quantify the propulsive force and moment sensitivity to angle-of-attack variation and elastic deflections of a representative hypersonic vehicle, and to assess the potential impact of these sensitivities on the vehicle's longitudinal flight dynamics. It is also intended to present a model useful for further investigations of the dynamics and control of a highly integrated hypersonic configuration.

Several recent studies have addressed aeroelastic-propulsive interactions for high-speed air-breathing vehicles. The specific challenge is relatively new in that the fuselage structure actually comprises major components of the propulsion system, namely, the aerodynamic compressor and nozzle. It is important to note that previous hypersonic aerospacecraft such as the Space Shuttle and the X-15 were not air-breathers, and so did not exhibit this specific form of aeroelastic-propulsive coupling. The SR-71 air-breathing propulsion systems were relatively self-contained and isolated from the fuselage, unlike the highly integrated propulsion elements of currently proposed aerospace plane concepts.

A recent investigation by Chan[3] addressed the problem of elastic interactions with the longitudinal dynamics of hypersonic aerospacecraft. The research suggested a potential control design solution that involved phase stabilization of a single structural mode by appropriately weighting and blending

Received March 8, 1993; presented as Paper 93-1367 at the AIAA/ASME/ASCE/AHS/ASC 34th Structures, Structural Dynamics, and Materials Conference, La Jolla, CA, April 19–21, 1993; revision received April 19, 1994; accepted for publication July 8, 1994.

*NASA Aerospace Researcher, Flight Dynamics and Control Division. Member AIAA.
†Technologist. Senior Member AIAA.

feedbacks from accelerometers placed fore and aft of an elastic node. However, the effect of fuselage deflections on propulsive forces and moments was not modeled in that study.

The potentially significant influence of such fuselage deflections on propulsion system transients, and the subsequent potential for interactions between propulsion system and elastic modes, was elaborated by Schmidt,[4,5] and further research was suggested. A study by Heeg et al.,[6] examined the aerothermoelastic characteristics of an air-breathing hypersonic configuration with engine nacelles located beneath the fuselage in an "underslung" combustor module. The model demonstrated the significant influence of aeroelasticity on the longitudinal pitch mode for this type of configuration, but did not include propulsion sensitivities to angle-of-attack or elastic fuselage deflections. The research presented in this report draws heavily upon the modeling efforts described by Heeg[6] and Spain,[7] and augments the aeroelastic model presented therein with propulsion system sensitivities to angle-of-attack variations and elastic fuselage deflections. Chavez and Schmidt[8] have recently attempted to derive analytical expressions for a complete set of aero-propulsive-elastic influence coefficients relating to a simplified model of an integrated flexible airframe and scramjet propulsion module. Predictions based on these analytical expressions will be compared with the model used in this investigation.

This report presents the results of an investigation that combined propulsive, aerodynamic, and structural modeling efforts to create a consolidated model of the longitudinal flight dynamics, propulsion system, and the first seven elastic modes of a representative air-breathing hypersonic configuration. First, the general characteristics of the subject configuration used in this study are described. Then the development of the aerodynamic, elastic, and propulsive elements of the math model is discussed and associated assumptions are noted. Estimates of the propulsion system sensitivity to angle-of-attack variations and modal fuselage deflections are then presented and compared to predictions based on expressions developed by Chavez.[8] Total force and moment variations in response to atmospheric turbulence are also quantified. The combined aeroelastic-propulsive model is then used to illustrate the sensitivity of the vehicle's rigid body pitch dynamics to nonlinearities in the propulsion sensitivities. A concluding section summarizes the implications of the observed effects for highly integrated hypersonic vehicle concepts.

Model Description

The configuration geometry, aeroelastic model, and propulsion model are described in the following sections. Simplifying assumptions associated with each of the models are noted. Numerical values for the completed aeroelastic-propulsive model at hypersonic flight conditions of Mach 6 and Mach 10 are also included.

Configuration

A three-view finite element representation of the vehicle concept used in this modeling effort is shown in Fig. 1. It is a hypersonic lifting body with lower surface engine nacelles, very similar in configuration to the proposed X-30 research vehicle.[9] This configuration was chosen because its design exhibits a high degree of airframe-propulsion integration, making it a good candidate for the study of aeroelastic-propulsive interactions.

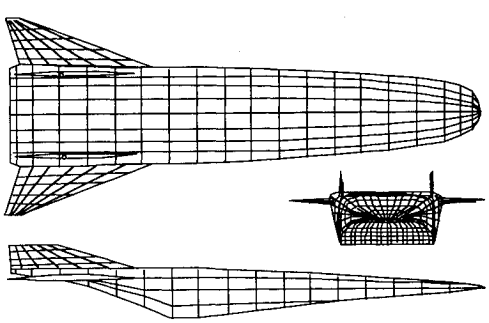

Fig. 1 Three-view finite element representation of subject configuration.

The vehicle length is 150 ft. The wingspan is 60 ft, with a wing sweep angle of 70 deg. Vertical fins project from the upper surface of the aft fuselage near the wing root. The configuration is equipped with all-moving wing control effectors. At hypersonic speeds, the lower surface of the elongated fuselage forebody acts as a compression wedge for the scramjet combustor unit, and the lower surface of the aft portion of the vehicle acts as a nozzle. The fuselage width at the combustor is 33.33 ft. The vehicle weight used in this study was 315,722 lb, and the pitch moment of inertia corresponding to this weight is 3.978×10^{10} lbm-in.^{2}.

The configuration was analyzed at two hypersonic flight conditions: 1) Mach 6 at 75,000 ft and 2) Mach 10 at 95,000 ft, representing two points along a typical ascent trajectory. The corresponding dynamic pressures are 1840 and 2010 psf, respectively, and the velocities relative to the air mass are 5845 and 9860 ft/s, respectively.

Aeroelastic Model

The aeroelastic model used in this investigation is derived from the work presented in Refs. 6 and 7. The state-space model is a longitudinal approximation. It includes seven symmetric bending modes and two rigid body degrees of freedom (DOF), consisting of pitch and vertical translation (plunge). No translational DOF along the vehicle's longitudinal axis is included. The general form of this aeroelastic model is shown in Eqs. (1) and (2):

$$\dot{x} = [A]x + [B]u \tag{1}$$

$$y = [C]\bar{x} \tag{2}$$

The state vector x contains a total of 21 elements; two for each of the seven second-order elastic modes, two for each of the rigid body DOF, and three states for an actuator model associated with the all-moving wing. The order of the elements in the state vector is given in Eq. (3), where a_{1-3} indicate the states of the third-order actuator model. The actuator model dynamics are identical to those used in Ref. 3:

$$x' = [h\theta\eta_1, \ldots, \eta_7 h\dot{\theta}\dot{\eta}_1, \ldots, \dot{\eta}_7 a_1 a_2 a_3] \tag{3}$$

The output vector y provides vertical displacements due to elastic deflection at 13 stations along the fuselage centerline. A positive deflection indicates an upward displacement. The order of elements in the output vector is given in Eq. (4), where δ_j indicates the elastic deflection at a specific location along the fuselage centerline. The subscript j of the element δ_j indicates the longitudinal fuselage station, measured in inches from the nose of the vehicle, at which that elastic deflection occurs. The displacements in y are obtained by multiplying $[C]$, by the vector of generalized coordinates $\bar{x}$, as shown in Eq. (2), where $\bar{x}$ is given in Eq. (5):

$$y' = [\delta_{47}\delta_{92}\delta_{158}\delta_{247}\delta_{336}\delta_{469}\delta_{646}\delta_{824}\delta_{1001}\delta_{1178}\delta_{1356}\delta_{1534}\delta_{1711}] \tag{4}$$

$$\bar{x}' = [\eta_1\eta_2\eta_3\eta_4\eta_5\eta_6\eta_7] \tag{5}$$

The input vector u contains one element corresponding to the angular deflection of the all-moving wing. $[B]$ is simply a scalar gain on the wing deflection to the first actuator state derivative. Therefore, $[B]$ is a column vector of 21 elements, with only the 19th element having a nonzero value where $B_{19} = 30.619$.

Table 1 Numerical values for C

Mode						
1	2	3	4	5	6	7
1.2792E−01	2.2066E−02	8.9420E−03	1.5091E−01	1.2901E−02	−1.7685E−01	1.2266E−01
1.1152E−01	1.8432E−02	6.8429E−03	1.1477E−01	9.2365E−03	−1.2916E−01	1.0552E−01
8.8377E−02	1.3456E−02	4.1273E−03	6.8195E−02	4.7269E−03	−7.1122E−02	8.3435E−02
6.0237E−02	7.6794E−03	1.2577E−03	1.9322E−02	3.8211E−04	−1.6338E−02	6.0107E−02
3.5212E−02	2.8463E−03	−8.3334E−04	−1.5852E−02	−2.3019E−03	1.6233E−02	4.2845E−02
3.5293E−03	−2.7242E−03	−2.7006E−03	−4.6320E−02	−3.8000E−03	3.2072E−02	2.6116E−02
−2.7046E−02	−6.9563E−03	−3.3847E−03	−5.8735E−02	−3.7861E−04	−2.8078E−02	1.5746E−02
−4.6125E−02	−8.5723E−03	−2.3608E−03	−3.6265E−02	1.6714E−03	−4.4902E−02	1.1270E−02
−5.3007E−02	−7.6459E−03	−4.2403E−04	3.8357E−03	2.1477E−03	−2.4011E−02	4.7274E−03
−4.6660E−02	−4.1231E−03	1.5815E−03	4.1884E−02	1.8206E−03	1.0353E−02	−1.1780E−02
−2.6055E−02	2.0499E−03	2.8117E−03	5.8193E−02	1.4604E−03	3.3948E−02	−4.6153E−02
9.8390E−03	1.0927E−02	2.4223E−03	3.3079E−02	1.8377E−03	2.2531E−02	−1.0629E−01
6.2052E−02	2.2563E−02	−4.3094E−04	−5.3144E−02	3.7226E−03	−4.8141E−02	−2.0009E−01

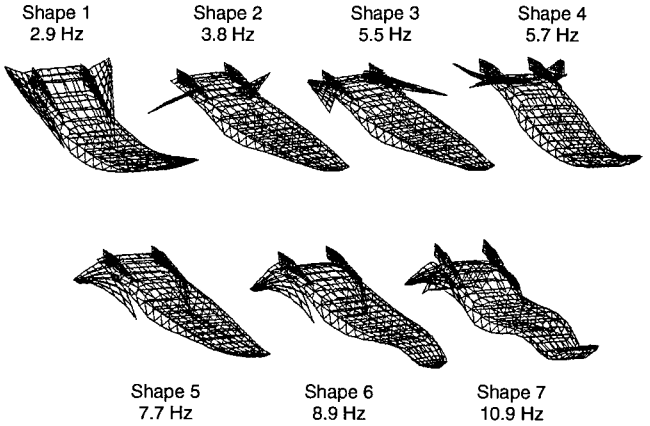

Fig. 2 Structural mode shapes and in-vacuo frequencies included in the aeroelastic model.

Numerical values for $[A]$ and $[C]$, appearing in Eqs. (1) and (2), were generated using the interaction of structures, aerodynamics, and controls code (ISAC).[10] A combination of Newtonian impact theory and Van Dyke's second-order piston theory was used to model the aerodynamic effects at the two selected hypersonic flight conditions. A complete description of the aeroelastic modeling process is presented in Refs. 6, 7, and 11.

The shapes and in-vacuo frequencies of the seven elastic modes included in this model are shown in Fig. 2. Each column of $[C]$ represents the structural displacements corresponding to a unit deflection of one of the elastic mode shapes shown in Fig. 2. Numerical values for the mode shape matrix are given in Table 1. Mode shapes that strongly impact the fuselage geometry are of particular importance, since they are likely to have the greatest influence on the propulsion system. Mode shapes 1, 4, 6, and 7 are predominantly fuselage bending modes, whereas shapes 2, 3, and 5 are wing deflections. The in-vacuo frequencies of the elastic modes are relatively low and closely spaced. Detailed elaboration on the character and significance of the various mode shapes is also provided in Refs. 6 and 7.

Propulsion Model

The hypersonic propulsion model was developed using the SRGULL code.[12] The SRGULL code uses a two-dimensional inviscid forebody and inlet analysis, and a one-dimensional combustor analysis to address the entire propulsion system flow path. A variable grid is used to analyze the vehicle "nose-to-tail" stream tube control volume, determining mass capture, forebody and inlet drag, and combustor and nozzle performance.

The nose-to-tail propulsion flow path consists of the undersurface of the fuselage forebody, the combustor, and the

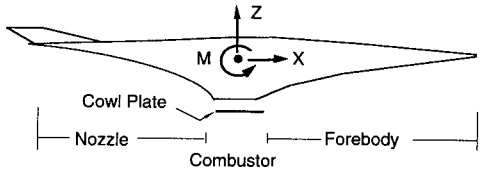

Fig. 3 Undersurface geometry of hypersonic vehicle analyzed using SRGULL.

undersurface of the fuselage aftbody, shown in Fig. 3. The forces and moments predicted by the code include the total aerodynamic and propulsive components acting on the fuselage, invoking the assumption from Newtonian impact theory that the upper surface is in leeward flow, wherein pressure coefficients are set to zero. The force and moment predictions from SRGULL do not include aerodynamic contributions from the wing or vertical tail surfaces. The coordinate system shown in Fig. 3 depicts the positive sign convention for X, Z, and M, that will be used in this report.

The SRGULL code also provides the option to remove the aerodynamic contribution of the fuselage forebody from the predicted forces and moments. The resulting coefficients include the effect of the propulsion cowl plate, combustor, and nozzle shown in Fig. 3, and are referred to as "cowl-to-tail" force and moment predictions in this report.

The SRGULL code was used to predict the sensitivity of axial force, normal force, and pitching moment to aeroelastic deflections and angle-of-attack variation. The code was first run at both flight conditions (Mach 6 and Mach 10) for the undeflected vehicle geometry over an angle-of-attack range from -1 to 3 deg in 1-deg increments. Then, at each angle of attack, small perturbations about the baseline geometry corresponding to each of the seven elastic mode shapes were analyzed. A finite difference method was then applied to the resulting data to obtain sensitivity coefficients for axial force, normal force, and pitching moment to each of the seven elastic mode shapes and angle of attack.

The coefficients obtained from the SRGULL data consist of Z_α, M_α, X_α, $Z_{\eta j}$, $M_{\eta j}$, and $X_{\eta j}$, where the subscript j varies from 1 to 7 to designate a particular elastic mode shape. It should be emphasized that this part of the analysis was performed using nose-to-tail predictions from SRGULL, so the resulting coefficients include the effect of both the aerodynamic and propulsive variation produced by the perturbed fuselage geometries for each mode shape. These coefficients will be compared with force and moment sensitivity predictions based on Ref. 8.

The SRGULL code was also used to quantify the force and moment variation that may occur in response to atmospheric turbulence. To achieve this, deflected geometries produced by turbulence inputs were analyzed at each angle of attack along with the undeflected baseline geometry. The turbulence-induced deflections were obtained from an rms response

of the aeroelastic model to a three-sigma von Kármán spectra turbulence input. The resulting force and moment variations are presented in the following section of this report.

The propulsion modeling approach used in this study neglects unsteady aerodynamic effects in the propulsion flow path. The impact of such effects on the magnitude of the propulsive perturbations arising from deformation of the forebody and nozzle are uncertain. The model presented in this report represents an idealized case in which fuselage deflections and angle-of-attack variations instantaneously produce propulsive perturbations. Fuel flow rate was held constant. Dynamics associated with the scramjet combustion process are assumed negligible. This is not an unreasonable assumption, since the time required for a fluid particle to traverse the 7-ft combustor flow path when the vehicle is traveling at Mach 6 would be approximately 0.001 s, whereas the highest frequency associated with the elastic modes included in the model is about 10.9 Hz (a period of 0.092 s).

Results and Discussion

The nose-to-tail force and moment predictions from SRGULL are plotted against angle of attack in Figs. 4–6. Solid symbols represent data for the undeflected vehicle geometry at Mach numbers of 6 and 10. The brackets about each symbol indicate the range of variation in axial force, normal force, or pitching moment resulting from analysis of the turbulence-induced perturbation geometries, as described in the preceding section.

The normal force data shown in Fig. 4 indicate a pronounced sensitivity to angle-of-attack variation. Lift force for the Mach 6 flight condition doubles over this 4-deg angle-of-attack range. The wide, flat forebody of the vehicle is the primary contributor to this trend. It should be noted that at an angle of attack of −1 deg, the forebody of this configuration still acts as a hypersonic compression wedge, generating positive lift. The lift curve appears virtually linear for the Mach 6 flight condition.

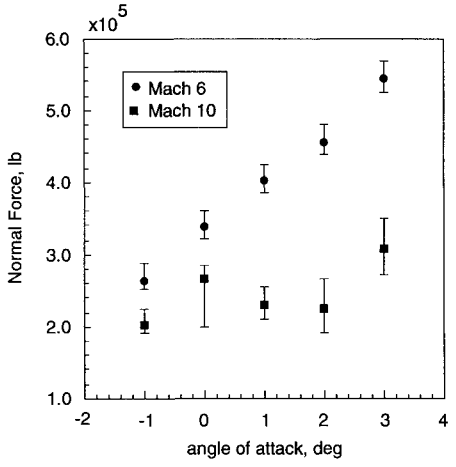

Fig. 4 Normal force variation with angle of attack.

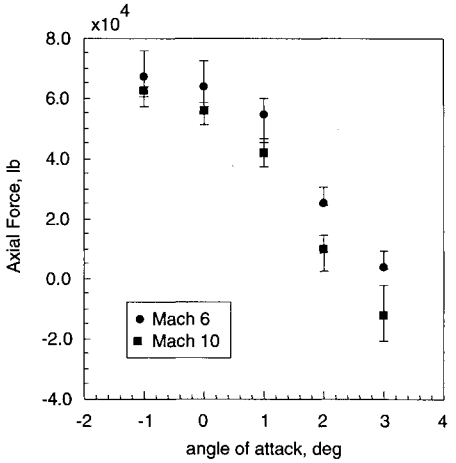

Fig. 5 Axial force variation with angle of attack.

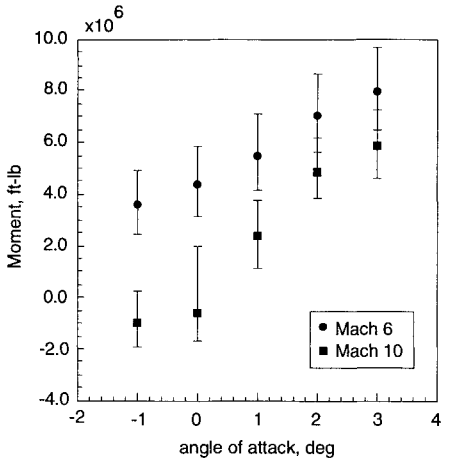

Fig. 6 Pitching moment variation with angle of attack.

However, in the Mach 10 case there is a significant variation in the trend of the lift curve slope. This variation is caused by a large downward force on the lower cowl plate of the scramjet combustor module, which cancels a significant portion of the lift force produced on the forebody. (The lower cowl plate is visible in Fig. 3 as a flat plate enclosing the bottom of the combustor section.) This effect is more pronounced in the Mach 10 case because a greater percentage of the total flow being turned by the forebody is captured by the combustor inlet and is being redirected by the combustor cowl plate. The data brackets in Fig. 4 indicate that fuselage deflections due to turbulence generally produced greater normal force variations in the Mach 10 case than in the Mach 6 case.

Axial force variation with angle of attack is shown in Fig. 5. A consistent downward trend in axial force (decreasing thrust) with increasing angle of attack is observed. The nose-to-tail data plotted in Fig. 5 includes the drag contribution from the vehicle forebody. The thrust produced by the scramjet and nozzle without the forebody drag contribution is actually greatest at an angle of attack of +1 deg. But drag contributed by the forebody overwhelms this trend, causing the greatest total axial force to occur at an angle of attack of −1 deg, since this is the lowest drag condition. From Figs. 4 and 5 it is apparent that the highest thrust condition is also the lowest lift condition for this configuration. The brackets in Fig. 5 indicate that considerable variations in axial force were produced by the turbulence-induced geometry perturbations.

Pitching moment variation with angle of attack is plotted in Fig. 6. The configuration is statically unstable in pitch at both flight conditions, as evidenced by the positive slope of the moment curves. Large variations in pitching moment were produced by the turbulence-induced deflections. The magnitude of these moment variations emphasizes the importance of sensor placement and associated signal filtering to avoid high levels of control activity in the presence of turbulence, and highlights the significance of the aeroelastic stabilization techniques presented by Chan.[3]

The range of variation observed in propulsive forces and moments corroborates the investigation by Walton,[1] which predicted a strong sensitivity of scramjet-propelled vehicles to angle of attack. The effect that unsteady aerodynamics would have on the turbulence-induced propulsive perturbations has been assumed small, but this is uncertain and no experimental data is available with which to confirm these predictions.

Prediction of Sensitivity Coefficients

Linearized force and moment sensitivity coefficients that were produced from the SRGULL data using the method described earlier in this report are shown in the first and second columns of Table 2. These coefficients were obtained using a nominal angle of attack of 2 deg as the linearization condition for the data base plotted in Figs. 4–6. The SRGULL coefficient predictions are for the Mach 6 and Mach 10 flight conditions. This data is compared with predictions based on the example presented by Chavez and Schmidt[8] for a similar configuration at Mach 8. The model used in Ref. 8 included an approximation for the first fuselage bending mode shape. Coefficients that are compared consist of force and moment sensitivities to angle-of-attack variation and the first fuselage bending mode. The units on these coefficients are as follows: Z_α (lb/rad), M_α (ft-lb/rad), X_α (lb/rad), $Z_{\eta 1}$ (lb/unit deflection), $M_{\eta 1}$ (ft-lb/unit deflection), and $X_{\eta 1}$ (lb/unit deflection). A combustor width of 33.3 ft was used with the example data in Ref. 8 to obtain these predictions. This data is presented in the third column of Table 2.

Table 2 Comparison of predicted sensitivity coefficients

Parameter	SRGULL predictions		Predictions based on Ref. 8,
	Mach 6	Mach 10	Mach 8
Z_α	8.1008e+04	6.8059e+04	1.3215e+05
M_α	1.0748e+06	1.1756e+06	2.4750e+06
X_α	−2.4040e+04	−2.4433e+04	−1.1983e+04
$Z_{\eta 1}$	4.2988e+02	6.1279e+02	1.5525e+03
$M_{\eta 1}$	2.6718e+04	2.1637e+04	7.2825e+04
$X_{\eta 1}$	−1.4462e+00	−6.1318e+01	5.8461e+01
$Z_{\eta 2}$	−6.5812e+01	−9.8116e+01	—
$M_{\eta 2}$	5.0377e+03	3.9845e+03	—
$X_{\eta 2}$	2.2461e+00	−5.4145e+00	—
$Z_{\eta 3}$	−2.7968e+01	−4.5914e+01	—
$M_{\eta 3}$	2.1569e+03	1.6998e+03	—
$X_{\eta 3}$	1.0144e+00	−2.7649e+00	—
$Z_{\eta 4}$	−4.7735e+02	−7.9632e+02	—
$M_{\eta 4}$	3.6736e+04	2.8941e+04	—
$X_{\eta 4}$	1.7168e+01	−4.9186e+01	—
$Z_{\eta 5}$	−4.3827e+01	−5.0269e+01	—
$M_{\eta 5}$	2.2318e+03	1.8684e+03	—
$X_{\eta 5}$	−1.4728e+00	−7.0374e+00	—
$Z_{\eta 6}$	6.5427e+02	6.3761e+02	—
$M_{\eta 6}$	−2.4174e+04	−2.1489e+04	—
$X_{\eta 6}$	4.6115e+01	1.3427e+02	—
$Z_{\eta 7}$	−5.2305e+02	−6.2789e+02	—
$M_{\eta 7}$	1.7701e+04	1.5880e+04	—
$X_{\eta 7}$	−4.0552e+01	−1.3024e+02	—

The two sets of predictions compare well in terms sign and order of magnitude. The comparison asserts the value of the analytical expressions presented in Ref. 8 for use in rapidly obtaining good approximations for the influence coefficients that describe this type of complex aeroelastic-propulsive interaction.

The SRGULL predictions were used to augment the aeroelastic $[A]$, produced by ISAC. This yielded a stability matrix that contained both aeroelastic and propulsive effects. The SRGULL cowl-to-tail predictions which include the effect of the propulsion cowlplate, combustor, and nozzle shown in Fig. 7, were used for this procedure. The cowl-to-tail predictions from SRGULL were used instead of the nose-to-tail predictions since the ISAC stability matrix already included the aerodynamic contribution of the vehicle forebody from Newtonian impact theory and Van Dyke's second-order piston theory. In this way it was possible to avoid double-bookkeeping the aerodynamic effect of the fuselage forebody. Figure 7 depicts the contributions from ISAC and SRGULL to the coefficients of the stability matrix. It should be emphasized that the SRGULL contributions do not contain unsteady aerodynamic effects.

$[A]$ of the completed aeroelastic-propulsive model is partitioned as shown in Eq. (6). The submatrices of $[A]$ have

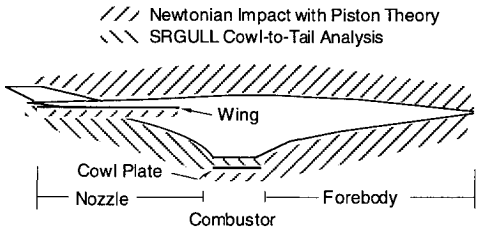

Fig. 7 Contributions from Newtonian impact theory and SRGULL to completed aeroelastic-propulsive model.

Table 3 Values of submatrix $A_{2,1}$ for Mach 6

Column								
1	2	3	4	5	6	7	8	9
−1.9950E−07	9.9152E+03	2.9494E−01	3.4020E+00	1.4641E−01	1.6394E+00	−1.2534E+00	−1.9323E+00	1.2607E+00
−9.2167E−10	3.2156E+00	4.8396E−03	−6.8347E−03	−9.3578E−06	1.3188E−03	6.2500E−03	−1.8878E−03	7.9811E−04
−1.5565E−05	1.5674E+04	−3.3728E+02	3.3342E+01	3.1284E+00	5.5928E+01	5.1461E+01	−8.9466E+00	2.9716E+01
−2.8394E−06	−2.8603E+04	1.8675E+01	−6.9408E+02	1.4264E+00	2.8017E+01	−1.2916E+02	−1.2575E+02	−3.8946E+01
−1.2313E−06	4.6229E+03	−2.9604E+00	1.6388E+01	−1.2070E+03	3.9295E+00	−8.7036E+00	−9.6192E+00	−8.0274E−01
−2.0854E−05	2.1182E+04	−1.8848E+01	1.2815E+02	4.3969E+00	−1.2588E+03	−4.8230E+01	−1.0672E+02	−7.0827E+00
−1.7937E−05	−1.0427E+05	7.4171E+01	−3.8917E+02	−9.4016E+00	−3.7825E+01	−2.0869E+03	1.5067E+02	5.1384E+01
2.3728E−05	−1.4982E+05	2.9227E+01	−2.1959E+02	−7.1902E+00	−5.8368E+01	1.1823E+02	−2.9793E+03	−1.1045E+00
−1.4134E−05	1.5050E+04	4.7804E+01	−2.1040E+01	1.4038E−01	−4.4119E+00	5.2566E+01	−5.7787E+01	−4.7468E+03

Table 4 Values of submatrix $A_{2,2}$ for Mach 6

Column								
1	2	3	4	5	6	7	8	9
−1.6946E−01	−2.6454E+01	−6.4765E−04	1.1302E−03	−1.9726E−04	−9.1205E−04	4.4672E−03	6.3521E−03	−6.2655E−04
−6.3734E−05	−1.8062E−01	−4.1838E−06	−6.2861E−06	4.7205E−07	2.1766E−06	−1.3243E−05	−1.6691E−06	−1.7597E−05
−2.6487E−01	−4.3122E+02	−7.5282E−01	1.7310E−01	−5.3227E−03	−6.9183E−02	−4.9666E−02	5.9158E−02	−2.5825E−02
4.6221E−01	−6.4791E+02	1.7310E−01	−1.8101E+00	−5.0866E−03	−4.0097E−02	1.1548E−01	6.0570E−02	−1.6283E−03
−8.0672E−02	4.8654E+01	−5.3227E−03	−5.0866E−03	−1.0445E+00	−1.9870E−02	3.4155E−02	2.5876E−02	1.1729E−03
−3.7300E−01	2.2435E+02	−6.9183E−02	−4.0097E−02	−1.9870E−02	−1.3199E+00	2.1506E−01	2.1244E−01	−5.3925E−02
1.8270E+00	−1.3649E+03	−4.9666E−02	1.1548E−01	3.4155E−02	2.1506E−01	−2.4900E+00	−4.8316E−01	−1.0416E−01
2.5978E+00	−1.7203E+02	5.9158E−02	6.0569E−02	2.5876E−02	2.1244E−01	−4.8316E−01	−2.1568E+00	−2.6876E−02
−2.5624E−01	−1.8137E+03	−2.5825E−02	−1.6283E−03	1.1729E−03	−5.3925E−02	−1.0416E−01	−2.6876E−02	−2.3539E+00

dimensions as follows: $A_{1,1}$, $A_{1,2}$, $A_{2,1}$, and $A_{2,2}$ are 9 × 9; $A_{1,3}$ and $A_{2,3}$ are 9 × 3; $A_{3,1}$ and $A_{3,2}$ are 3 × 9; and $A_{3,3}$ is 3 × 3:

$$[A] = \begin{bmatrix} A_{1,1} & A_{1,2} & A_{1,3} \\ A_{2,1} & A_{2,2} & A_{2,3} \\ A_{3,1} & A_{3,2} & A_{3,3} \end{bmatrix} \tag{6}$$

where $A_{1,1} = [0]$, $A_{1,2} = [I]$, $A_{1,3} = [0]$, $A_{3,1} = [0]$, and $A_{3,2} = [0]$ at both the Mach 6 and Mach 10 flight conditions. Numerical values for the remaining submatrices of $[A]$ at the Mach 6 flight condition are presented in Tables 3–6. The analogous values for the Mach 10 flight condition are presented in Tables 7–9. These numerical models were used to investigate the impact of the SRGULL propulsion sensitivities on the vehicle's rigid body pitch mode.

Table 5 Values of submatrix $A_{2,3}$ for Mach 6

Column		
1	2	3
2.5048E+04	−2.3848E+04	−4.6609E+01
−1.3305E+02	1.3034E+02	2.4628E−01
4.3728E+06	−4.3634E+06	−8.0662E+03
−2.3299E+07	2.3268E+07	4.2969E+04
−1.5620E+05	1.6211E+05	2.8638E+02
−8.6636E+05	9.1233E+05	1.5821E+03
4.0898E+06	−4.2298E+06	−7.4956E+03
2.0938E+06	−2.1708E+06	−3.8367E+03
8.7783E+04	−9.7524E+04	−1.5960E+02

Table 6 Values of submatrix $A_{3,3}$ for Mach 6 and Mach 10

Column		
1	2	3
−3.0619E+01	0.0000E+00	0.0000E+00
0.0000E+00	0.0000E+00	1.0000E+00
7.4474E+04	−7.4474E+04	−1.3850E+02

Impact on Longitudinal Flight Dynamics

Eigenvalues of the augmented stability matrix for the Mach 6 and Mach 10 aeroelastic-propulsive models are indicated by the square symbols shown in Figs. 8a and 8b. The eigenvalues that lie off the real axis correspond to the seven elastic mode shapes shown in Fig. 2. The square symbols lying on the real axis denote this vehicle's statically unstable pitch mode. The scales of the real and imaginary axes have been adjusted to provide better resolution of the poles lying on the real axis. The solid triangular symbols in Figs. 8a and 8b indicate the poles of the short period and first elastic modes for the example vehicle used in Refs. 8 and 13 at Mach 8. Good agreement with the poles of the combined ISAC/SRGULL model is apparent.

It was found that the eigenvalues of the pitch mode of the stability matrices given in Eqs. (7–9) varied with the angle of attack chosen as the linearization condition for the propulsion sensitivity coefficients. (Recall that the linearization angle of attack for the coefficients presented in Table 2 was 2 deg.) The plus symbols in Figs. 8a and 8b indicate the eigenvalues of the stability matrices when the nominal angle of attack was varied from −1 to 3 deg in 1-deg increments. A greater range of short period characteristics resulted for the Mach 10 condition due to the nonlinearity of the force and moment variation with angle of attack shown in Figs. 4–6.

The solid bars below the real axis in Figs. 8a and 8b quantify the range of variation (in rad/s) produced by changing the angle of attack used as the linearization condition for the propulsion model. Considerable variation in predicted short period dynamics is possible depending upon the linearization condition chosen for the propulsion model. The magnitude of this variation illustrates the significant impact of the propulsion characteristics on the rigid body pitch dynamics.

The eigenvalues of the seven elastic modes were not altered by the variation in propulsion sensitivities due to changing the propulsion linearization condition. This is primarily because the SRGULL code could not provide predictions for the sensitivities of the elastic states to angle-of-attack variations and aeroelastic deflections (derivatives such as η_{i_α} and $\eta_{i_{\eta_j}}$). Therefore the effect of the propulsion sensitivities on

Table 7 Values of submatrix $A_{2,1}$ for Mach 10

Column								
1	2	3	4	5	6	7	8	9
−9.3420E−08	3.1821E+03	9.7999E−01	1.4955E+00	1.0823E−01	1.3923E+00	−1.4641E−01	−1.2551E+00	5.4887E−01
−4.5563E−10	4.7025E+00	1.7610E−03	−2.6009E−03	2.9555E−05	1.3377E−03	2.8180E−03	−9.0963E−04	1.5754E−03
−8.0748E−06	7.9721E+03	−3.3637E+02	7.0622E+00	1.2124E+00	2.2335E+01	2.9475E+01	−1.1214E+01	1.1714E+01
−1.4916E−06	−1.8023E+03	1.9323E+00	−5.9240E+02	1.4097E+00	1.4444E+01	−6.9104E+01	−6.4179E+01	−1.9073E+01
−6.5752E−07	1.2116E+03	−1.1363E+00	7.1886E+00	−1.2073E+03	1.8616E+00	−3.8967E+00	−4.6557E+00	−5.8529E−01
−1.1147E−05	−2.4921E+03	−6.6960E+00	5.4505E+01	2.1999E+00	−1.2729E+03	−2.0385E+01	−4.8683E+01	−3.6885E+00
−9.6396E−06	−5.3628E+04	3.4741E+01	−1.6761E+02	−4.2230E+00	−1.9022E+01	−2.2347E+03	6.7206E+01	2.1439E+01
1.2680E−05	−7.3178E+04	1.1465E+01	−9.5893E+01	−3.2583E+00	−2.6085E+01	5.3287E+01	−3.0377E+03	2.0684E−01
−7.2828E−06	5.2589E+04	1.2526E+01	−1.1509E+01	7.6787E−01	1.7859E+01	2.3164E+01	−1.4302E+01	−4.7168E+03

Table 8 Values of submatrix $A_{2,2}$ for Mach 10

Column								
1	2	3	4	5	6	7	8	9
−2.6792E−02	−1.2048E+01	−1.6122E−04	2.0720E−05	−2.5531E−05	4.6480E−05	1.1210E−03	1.5155E−03	−1.0800E−03
−3.9470E−05	−3.5119E−02	−1.6470E−06	−7.9972E−07	6.9518E−08	1.6421E−07	−3.2057E−06	−6.2456E−08	−2.4036E−06
−6.5935E−02	−1.6975E+02	−5.9592E−01	2.8514E−02	−1.3462E−03	−2.2274E−02	−1.6115E−02	9.5295E−03	−1.8893E−02
8.4737E−03	−8.2428E+01	2.8514E−02	−9.1386E−01	−1.9310E−03	−1.8062E−02	4.9394E−02	2.7333E−02	−3.1262E−03
−1.0441E−02	7.1652E+00	−1.3462E−03	−1.9310E−03	−1.0429E+00	−4.2648E−03	7.4018E−03	6.0475E−03	−2.3499E−04
1.9009E−02	1.6925E+01	−2.2274E−02	−1.8062E−02	−4.2648E−03	−1.1270E+00	4.4285E−02	5.5675E−02	−1.1964E−02
4.5845E−01	−3.3041E+02	−1.6115E−02	4.9394E−02	7.4018E−03	4.4285E−02	−1.6850E+00	−1.0203E−01	−3.2378E−02
6.1978E−01	−6.4374E+00	9.5295E−03	2.7333E−02	6.0475E−03	5.5675E−02	−1.0203E−01	−1.7748E+00	1.8408E−03
−4.4169E−01	−2.4774E+02	−1.8893E−02	−3.1262E−03	−2.3499E−04	−1.1964E−02	−3.2378E−02	1.8408E−03	−2.0843E+00

Table 9 Values of submatrix $A_{2,3}$ for Mach 10

Column		
1	2	3
2.5048E+04	−2.4575E+04	−4.6681E+01
−1.3305E+02	1.3202E+02	2.4743E−01
4.3728E+06	−4.3715E+06	−8.1206E+03
−2.3299E+07	2.3299E+07	4.3264E+04
−1.5620E+05	1.5879E+05	2.8932E+02
−8.6636E+05	8.8587E+05	1.6022E+03
4.0898E+06	−4.1507E+06	−7.5741E+03
2.0938E+06	−2.1276E+06	−3.8769E+03
8.7783E+04	−9.2237E+04	−1.6173E+02

□ Combined aeroelastic-propulsive model, $\alpha_0 = 2$ degrees
▲ Pitch mode and first elastic mode for example in Ref. 8, 13
\+ Pitch modes for α_0 = -1, 0, 1, 2, 3 degrees
━ Range of variation in pitch mode due to varied linearization conditions (rad/sec)

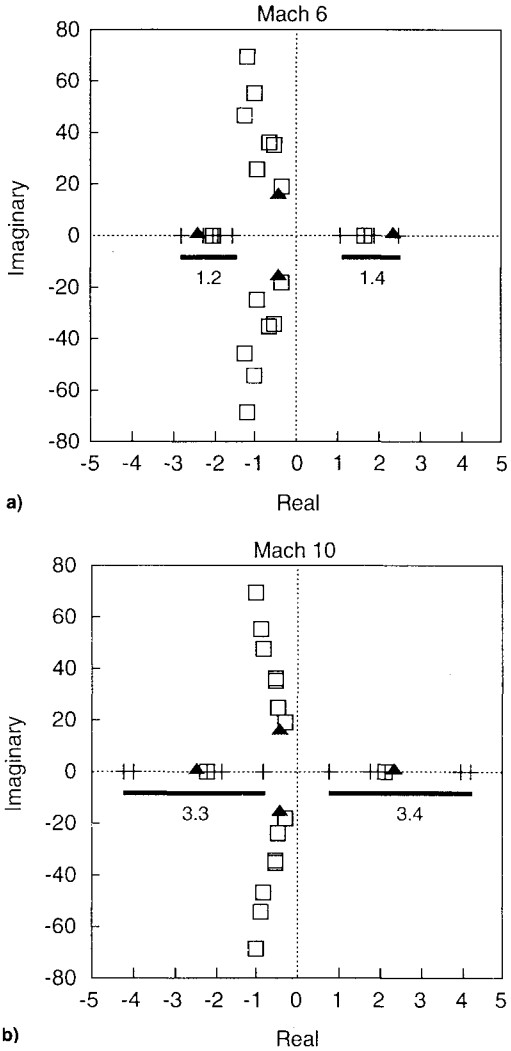

Fig. 8 Eigenvalues of stability matrix for a) Mach 6 and b) Mach 10.

the elastic modes cannot be assessed by the method used in this investigation. Whether or not the characteristics of the aeroelastic modes would be significantly altered by the propulsion system sensitivities is an issue that requires further study.

The impact of the propulsion sensitivities on the rigid body pitch mode has significant implications for the control of hypersonic air-breathers. It is likely that these effects would adversely impact the operation of a controller designed to stabilize the vehicle's longitudinal flight dynamics, if they were not taken into account in the control design process. It is important to emphasize the geometry-dependence of these results. The subject vehicle uses a lower surface propulsion module ("underslung"). It is possible that a wrap-around engine nacelle configuration would exhibit a different trend in the magnitudes of the propulsion sensitivities and their impact on the rigid body dynamics. It is also possible that an actively controlled combustor inlet geometry could be designed for an underslung configuration to reduce the propulsion system sensitivity to aeroelastic fuselage vibrations.

Concluding Remarks

This investigation has determined propulsion system sensitivities to angle-of-attack variations and aeroelastic fuselage deflection for an air-breathing hypersonic vehicle. The configuration was a lifting body with a highly integrated scramjet propulsion module located on the lower surface of the fuselage. The vehicle was analyzed at flight conditions of Mach 6 and Mach 10. Substantial force and moment sensitivities to elastic fuselage deflections were predicted. This sensitivity is introduced by the basic propulsion-airframe integration design concept that utilizes the fuselage undersurface as an aerodynamic compression wedge for the hypersonic propulsion system. Results compared well with predictions based on an earlier study. Significant force and moment variations arising from turbulence-induced fuselage deflections were also predicted. Numerical values for the completed state-space model were presented.

The propulsion sensitivity data was used to augment an existing aeroelastic model. The nonlinearity of the propulsive forces and moments with angle of attack introduced a range of possible rigid body pitch dynamics that could be exhibited by the combined aeroelastic-propulsive system. This range was expressed as a quantifiable uncertainty associated with the characteristics of the rigid body pitch mode. The magnitude of this uncertainty highlights the need for robust control to manage the complex dynamic interactions that will exist in a vehicle of this type. The geometry dependence of these results was emphasized since the configuration used in this study incorporated a lower surface propulsion module, and it is possible that a wrap-around engine nacelle configuration would exhibit different characteristics.

There is a need for experimental data to validate the predictions of propulsion system sensitivities to angle-of-attack variations and elastic deflections. Further research is also needed to assess the effect of unsteady aerodynamics on the propulsion system sensitivities. The model used in this investigation was suitable to assess the impact of propulsion system sensitivities on the vehicle's rigid body pitch mode, but further work is needed to assess their impact on the stability characteristics of the vehicle's elastic modes.

References

[1]Walton, J., "Performance Sensitivity of Hypersonic Vehicles to Changes in Angle of Attack and Dynamic Pressure," AIAA Paper 89-2463, July 1989.

[2]McRuer, D. T., "Design and Modeling Issues for Integrated Airframe/Propulsion Control of Hypersonic Flight Vehicles," *American Control Conference Proceedings* (Boston, MA), 1991.

[3]Chan, S. Y., Cheng, P. Y., Pitt, D. M., Myers, T. T., Klyde, D. H., Magdaleno, R. E., and McRuer, D. T., "Aeroservoelastic Stabilization Techniques for Hypersonic Flight Vehicles," NASA CR 187614, Sept. 1991.

[4]Schmidt, D. K., Mamich, H., and Chavez, F., "Dynamics and Control of Hypersonic Vehicles—The Integration Challenge for the 1990's," AIAA Paper 91-5057, Dec. 1991.

[5]Schmidt, D. K., "Dynamics and Control of Hypersonic Aeropropulsive/Aeroelastic Vehicles," AIAA Paper 92-4326, Aug. 1992.

[6]Heeg, J., Zeiler, T. A., Pototzky, A. S., Spain, C. V., and Engelund, W. C., "Aerothermoelastic Analysis of a NASP Demonstrator Model," AIAA Paper 93-1366, April 1993.

[7]Spain, C., Zeiler, T., Gibbons, M., Soistmann, D., Pozefsky, P.,

DeJesus, R., and Brannon, C., "Aeroelastic Character of a National Aerospace Plane Demonstrator Concept," AIAA Paper 93-1314, April 1993.

[8]Chavez, F., and Schmidt, D. K., "An Integrated Analytical Aeropropulsive/Aeroelastic Model for the Dynamic Analysis of Hypersonic Vehicles," AIAA Paper 92-4567, Aug. 1992.

[9]Kandebo, S. W., "JPO Studying Flight Test Issues in Early Phases of X-30 Program," *Aviation Week and Space Technology*, Oct. 29, 1990, pp. 46, 47.

[10]Tiffany, S. H., Adams, W. M., Jr., and Silva, W. A., *ISAC v5.1—Interaction Structures, Aerodynamics, and Controls*, NASA TM-100666, Jan. 1992.

[11]Pototzky, A. S., Zeiler, T. A., Noll, T. E., Whitlow, W., Heeg, J., and Scott, R. C., "Aeroservothermoelasticity, an Interim Review of NASP," NASP CR 1135, Aug. 1992.

[12]Walton, J. T., "Program SRGULL," COSMIC, Univ. of Georgia, LEW-15093, Athens, GA, May 1990.

[13]Chavez, F., and Schmidt, D. K., "Dynamics of Hypersonic Flight Vehicles Exhibiting Significant Aeroelastic and Aeropropulsive Interactions," AIAA Paper 93-3763, Aug. 1993.